Optics Letters

# Lab-on-a-chip optical biosensor platform: a micro-ring resonator integrated with a near-infrared Fourier transform spectrometer

Kyoung Min Yoo,[1,*] Kang-Chieh Fan,[1] May Hlaing,[2] Sourabh Jain,[1] Shupeng Ning,[1] Yue An,[1] and Ray T. Chen[1,2,3]

[1]Department of Electrical and Computer Engineering, The University of Texas at Austin, 10100 Burnet Rd., Austin, Texas 78758, USA
[2]Omega Optics Inc., 8500 Shoal Creek Blvd., Bldg. 4, Suite 200, Austin, Texas 78757, USA
[3]chenrt@austin.utexas.edu
*yoo_eb@utexas.edu

Received 4 April 2023; revised 28 August 2023; accepted 21 September 2023; posted 26 September 2023; published 10 October 2023

**In this paper, we demonstrated the design and experimental results of the near-infrared lab-on-a-chip optical biosensor platform that monolithically integrates the MRR and the on-chip spectrometer on the silicon-on-insulator (SOI) wafer, which can eliminate the external optical spectrum analyzer for scanning the wavelength spectrum. The symmetric add-drop MRR biosensor is designed to have a free spectral range (FSR) of ~19 nm and a bulk sensitivity of ~73 nm/RIU; then the drop-port output resonance peaks are reconstructed from the integrated spatial-heterodyne Fourier transform spectrometer (SHFTS) with the spectral resolution of ~3.1 nm and the bandwidth of ~50 nm, which results in the limit of detection of 0.042 RIU.** 

https://doi.org/10.1364/OL.492172

As the needs of the accurate and fast point-of-care portable biodetection systems are growing rapidly for the clinical and health-monitoring applications, various micro- and nanoscale optical biosensors have intrigued a significant attention as compact, highly selective, and sensitive real-time biosensor platforms [1]. Among them, micro-ring-resonator (MRR)-based optical sensors have been demonstrated in numerous applications due to their advantages of high sensitivity and small footprint compared to other photonic biosensor platforms [1–4]. Several researches have presented highly sensitive MRR biosensing applications in a near-infrared wavelength with advanced structures including sub-wavelength grating-based waveguides [5,6] and cascaded resonators utilizing Vernier effects [7–9] to maximize the sensing sensitivity, but utilizing external optical spectrum analyzer (OSA) was inevitable to read the spectrum and detect a resonance wavelength shift ($\Delta\lambda$) in any case, which makes the overall system bulky and expensive eventually. To miniaturize the whole system into a chip for the actual lab-on-a-chip biosensor, the integration of MRR and on-chip spectrometer that benefits from the photonic integrated circuits is highly demanded; by monolithically integrating the MRR with the on-chip spectrometer, it is able to remove the fiber coupling alignment or any other moving components between the resonator and the spectrometer, which makes the device safe from the environmental perturbations, in turn providing more reliable, robust, and low-cost advantages.

Several on-chip spectrometers have been demonstrated including the dispersive optics-based spectrometers [10–14], Fourier transform spectrometers (FTS) [15–23], and active tuning (electro/thermo-optic)-based spectrometers [24–26]; for the point-of-care (PoC) portable biosensing applications, which can read the spectrum in real time, a high-speed on-chip spectrometer based on the PICs is necessary, which makes the FTS an attractive solution that measures the spectrum with the interference of light instead of dispersion in a single capture, offering the advantages of a larger SNR and a faster data collection speed. Among the on-chip FTS schemes, the spatial-heterodyne-FTS (SHFTS) consists of an array of unbalanced Mach–Zehnder interferometers (MZIs) with linearly increasing optical path differences (OPDs), and the input spectrum can be reconstructed by Fourier transforming the output power interferogram measured from the MZI output arrays in a single capture without any active modulator or moving components [17].

The silicon-on-insulator (SOI) with the buried $SiO_2$ cladding is the most matured and attractive material platforms for the photonic biosensors because of the possibilities of scalable-mass production and compatibilities with a covalently attached functionalization layer coating [27]. In this work, we designed the MRR biosensors integrated with the on-chip SHFTS device using the CMOS compatible SOI wafer and experimentally demonstrated the resonance shift retrieval results from the fabricated SHFTS-MRR device in C-band.

The basic device configuration and working principle are demonstrated in Fig. 1. The MRR is a biosensing device which configures the resonance peaks from the drop-port output, and the evanescent field is altered when the molecular binding takes place between the immobilized bioreceptors and target analytes in the sample which changes the resonance condition leading to a resonance wavelength shift ($\Delta\lambda$). The drop port of MRR is directly connected to the SHFTS that is composed of an array of unbalanced MZIs with linearly increasing optical path delays ($\Delta L_i$). The phase change from each MZI is converted into an intensity change based on interferometric schemes, constituting the interferogram of the output powers. Output powers from

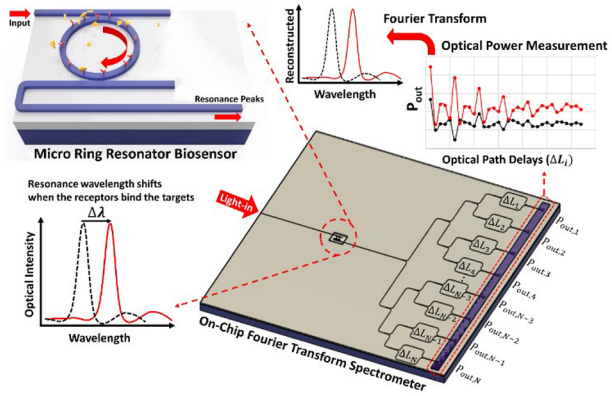


**Fig. 1.** Schematic illustration of the operation principle of the on-chip spectrometer integrated optical biosensor platform.

each MZI can be measured by the integrated photodetector (PD) array [28], and the input spectrum from the MRR drop port is reconstructed through the discrete Fourier transform equation (DFT) using the computation program, such as MATLAB. The center operation wavelength is 1550 nm, and the layer thicknesses of the SOI wafer and the strip waveguide are designed for guiding the fundamental transverse-electric (TE) mode based on previous researches [5,6,29]; the width and thickness of the silicon strip waveguide are 500 and 220 nm, respectively [5,6]; and the thickness of the SiO2 bottom cladding is ~3 μm, which is optimized for the grating coupler design for the fundamental TE mode based on the previous focusing sub-wavelength grating coupler (SWGC) structures [29].

Generally, the bulk-sensing sensitivity ($S$) of the MRR biosensor is defined as [3]

$$S = \frac{\Delta\lambda}{\Delta n_{\text{clad}}}, \tag{1}$$

where $\Delta\lambda$ is the resonance wavelength shift and $\Delta n_{\text{clad}}$ is the change of the cladding refractive index. Also, the limit of detection (LOD) of the sensor depends on the minimum resolvable wavelength shift that is determined by the measurement setup [3]:

$$\text{LOD} = \frac{\Delta\lambda_{\min}}{S}. \tag{2}$$

Here, $\Delta\lambda_{\min}$ is the minimum detectable resonance wavelength shift, which is the optical spectrum analyzer's measurement resolution ($\delta\lambda$). To maximize the sensing sensitivity, various waveguide structures and polarization effects have been studied, including the strip waveguide, slot waveguide [30], and sub-wavelength grating waveguide [5,6] with TE or TM (transverse-magnetic) mode. Essentially, the more interaction between the light and claddings (analytes), the higher the sensing sensitivity, but the optical losses are increasing at the same time, which hinder to achieve high-quality resonance peaks [3]. Hence, a good compromise between the MRR sensing sensitivity and the optical loss of the structure has to be considered [31]. However, regardless of the MRR sensitivity-improving strategies, this work focuses on the integration of MRR biosensor devices and SHFTS for the monolithic integration of the sensor and the spectrometer for the sensing-reading system integration, and we designed the basic symmetric add-drop ring-resonator device based on the strip waveguide with fundamental TE polarization.

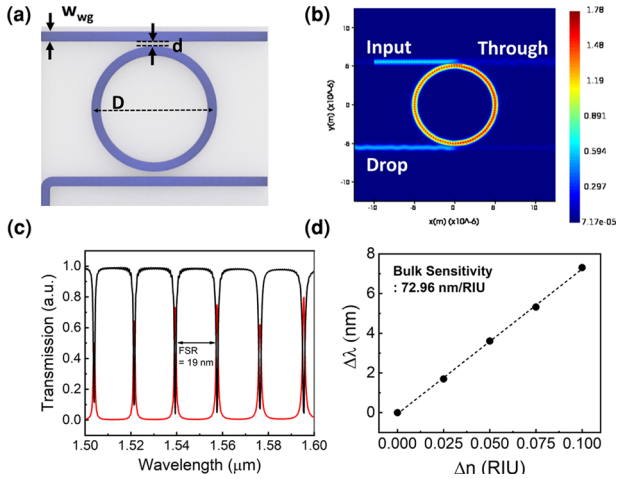


**Fig. 2.** (a) MRR biosensor design. (b) Electric-field simulation at a resonance peak. (c) Transmission spectrum from the through port and drop port; black line, through port; red line, drop port. (d) Resonance wavelength shift based on the refractive index change of the top cladding.

The design parameters include the gap distance (d) between the bus waveguide and ring waveguide to ensure the critical coupling based on the couple mode theory [32], and the diameter of the ring resonator (D) is designed to get the large enough FSR to make it compatible with the SHFTS spectral bandwidth coverage. The FSR, which is the wavelength range between two resonances, can be calculated as follows [2]:

$$\text{FSR} = \frac{\lambda^2}{n_g L}, \tag{3}$$

where $n_g$ is the group index of the waveguide and the L is the round-trip length of the ring waveguide. Another important optical characteristic of the MRR is the quality factor ($Q$), which is a measure of the sharpness of the resonance peak that is defined as follows [2]:

$$Q = \frac{\lambda_{\text{res}}}{\text{FWHM}}, \tag{4}$$

where $\lambda_{\text{res}}$ is the resonance wavelengths and FWHM is the full width at half maximum of the resonance spectrum.

The schematic illustration of the symmetric add-drop MRR device is shown in Fig. 2(a), and the device parameters are optimized by the three-dimensional (3D) finite-difference time-domain (FDTD) simulation, as d = 70 nm and D = 10 μm. For the MRR performance characterization, the transmission spectrum of the fabricated MRR device was measured using the OSA directly first, and the experimental measurement results with different d values were shown in Fig. S2 in Supplement 1. The top view of the E-field simulation result at the resonance peak is shown in Fig. 2(b), showing that the incident field at the resonance wavelength is transmitted to the drop port. The transmission spectrum of the drop and through ports is monitored by the 3D FDTD simulation [Fig. 2(c)], and the optical characteristics are measured as FSR = 19 nm, and Q ≅ 4000 from an optimized structure. Then, the refractive index of the top cladding is changed ($\Delta n_{\text{clad}}$) and the resonance wavelength shift ($\Delta\lambda$) is measured to calculate the bulk-sensing sensitivity of the biosensor that is presented in Fig. 2(d). The bulk-sensing sensitivity is calculated as S = 72.96 nm/RIU.

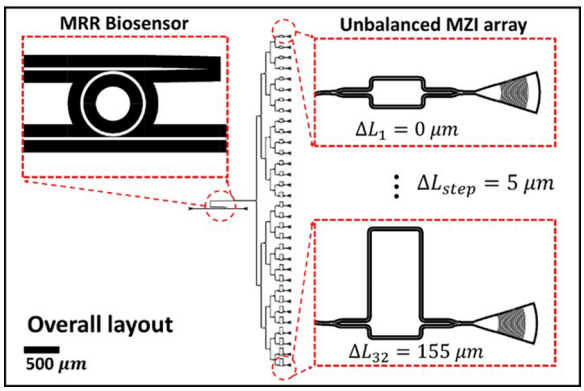


**Fig. 3.** Overall layout of the MRR-SHFTS integrated biosensor device.

The theory and principle of the standard SHFTS have been demonstrated by Florjańczyk *et al.* [17] and described in Supplement 1. For the biosensing application integrated with MRR, the spectrometer should be able to read and distinguish the separated resonance peaks by the FSR completely.

Accordingly, the silicon SHFTS is designed to reconstruct the resonance peaks from the optimized MRR shown in Fig. 2, in turn to have at least ~40 nm of bandwidth to retrieve at least two resonance peaks without aliasing errors, and the resolution is designed to be smaller than ~5 nm to make sure to resolve each peak separated by FSR clearly. Based on the SHFTS design principle, the silicon SHFTS is designed to have 32 MZIs (N = 32) with the maximum path length delay (ΔL) of 155 μm, which gives us the spectral bandwidth of 50 nm and the resolution of 3.1 nm, respectively. Subsequently, the LOD of the MRR-SHFTS integrated sensor is calculated as LOD = 0.042 RIU by Eq. (2), which is the minimum detectable refractive index change of the top cladding ($\Delta n_{clad}$). At this point, compared to the conventional OSA which typically provides the wavelength resolution of ±0.02 nm, the resolution of the SHFTS has to be improved to enhance the LOD of the biosensor; however the resolution of the standard SHFTS is highly limited by the number of MZIs (N) [21]; in order to achieve an ~30 pm resolution while maintaining the bandwidth of 50 nm, approximately 3200 MZIs are required, which make the size of the device significant. Instead of having an outrageous number of MZIs, several studies have proposed utilizing the active photonic components introducing the thermal/electrical optical phase delay [21–25].

Our prototype device focuses on the proof of concept of the sensor–spectrometer integration, and we used the SWGC [27] for coupling the input light source and collecting the powers from the MZI outputs, and the final device layout is presented in Fig. 3, which shows the fully integrated MRR biosensors and the SHFTS device. Based on the optimized designs, we have fabricated the devices. The detailed fabrication process is described in Supplement 1, and the optical microscope images of the fabricated MRR-SHFTS device including the overall layout and the SEM images of SWGC and MRR are shown in Fig. S1 in Supplement 1.

For testing, the transmission spectrum of the fabricated MRR device was measured using the OSA directly. Figure 4(a) shows the measurement setup. The NIR broadband light source (ASE-FL7001P) emits the light with a wavelength from 1.52 to 1.64 μm and coupled to the input SWGC through the single-mode fiber (SMF). Then, the MRR output spectrum is collected from the output through- and drop-port SWGCs through another SMF

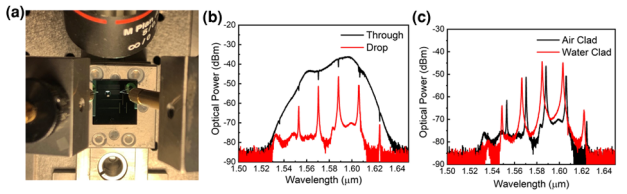


**Fig. 4.** MRR measurement results. (a) Measurement setup picture; water droplet is placed on top of the MRR. (b) OSA measurement results from the through and drop ports with air cladding. (c) OSA measurement results from the drop port with air and water cladding.

and measured by the OSA. Figure 4(b) shows the MRR output spectrum measurement results, including the through and drop ports; the envelope shape of the through-port signal is determined by the SWGC coupling. As a result, we measured the FSR = 19 nm and Q ≅ 4000 from the experimental results.

Next, we tested the resonance wavelength shift due to refractive index changes from the air and water cladding on top of the MRR device experimentally. Figure 4(c) shows the measured spectrum from the drop port with air and water cladding with $\Delta\lambda$ = 16 nm.

Then, the fabricated SHFTS device was tested with the tunable laser source to calibrate the FTS constants and validate the spectrum reconstruction performance. The tunable laser source (CoBrite DX4 from ID Photonics GmbH) provides the monochromatic signal with the tunable wavelength ranging from 1530 to 1567 nm, with the output power of ~250 μW measured from the SMF. We measured the output powers from each MZI with the wavelengths of 1550, 1555 and 1560 nm, respectively, which are shown in Fig. S3 in Supplement 1.

Based on the measured interferograms, we reconstructed the optical spectrum of each monochromatic signal by the MATLAB code based on the DFT equation, and the results are shown in Fig. 5. To validate the spectrum retrieval accuracy, the FTS retrieved results (black dashes) were compared with the direct OSA measurement results (red lines).

The wavelength positions of the FTS reconstructed spectra are well matched with the direct OSA measurement results, but the resolution of SHFTS is limited to ~3.1 nm, which result in a broader shape in reconstructed spectrum, and the discrepancies and ripples from the reconstructed spectrum are mainly due to the optical phase errors induced from the etching surface and the sidewall roughness.

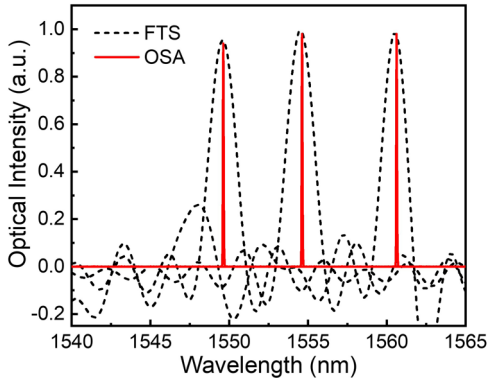


**Fig. 5.** Reconstructed spectrum of the tunable laser source at 1550, 1555, and 1560 nm; red line, OSA measurements; black dash: FTS reconstructed.

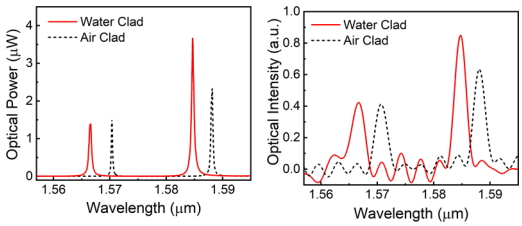


**Fig. 6.** MRR-SHFTS measurement result. (a) An OSA measured spectrum of the MRR drop port. (b) An FTS reconstructed spectrum.

Finally, by integrating the MRR biosensor and SHFTS, we reconstructed the drop-port output signals of the MRR by SHFTS and read the resonance wavelength shift with different claddings. The resonance peaks from the MRR drop ports shown in Fig. 4(c) are the polychromatic input signals of SHFTS, which can be considered as a superposition of monochromatic constituents, creating a corresponding spatial interferogram pattern formed by a superposition of the respective periodic $P_i^{out}$ fringes from the monochromatic input. The measured output powers with water and air cladding are shown in Fig. S4 in Supplement 1. Then, following the same DFT equation, the spectrum from the MRR with different claddings are reconstructed and compared with the direct MRR spectrum measurement results by OSA as shown in Fig. 6.

Figure 6(a) shows the MRR drop-port spectrum measurement results by OSA with different claddings, and Fig. 6(b) shows the SHFTS-MRR reconstructed spectrum. As the FTS reconstructed spectrum shows well-matching results with the direct OSA measurement results, we were able to validate that the MRR-SHFTS integrated device can successfully substitute the external OSA for the lab-on-a-chip biosensor applications. However, the resolution of the current SHFTS configuration is limited to ~3 nm, which limits the LOD = 0.042 RIU. To enhance the limit of detection, both the sensing sensitivity of the MRR [5–9] and the resolution of the SHFTS [21–25] can be improved, and we expect to improve the LOD by applying SWG-MRR sensors that we previously reported with S = 545 nm/RIU [5] that gives LOD = 0.0057 RIU.

In conclusion, we experimentally demonstrated the integration of the MRR biosensor and the on-chip SHFTS device for the lab-on-a-chip biosensor platform. The symmetric add-drop MRR is designed to have FSR = 19 nm, Q ≅ 4000, and S = 72.9 nm/RIU, and the SHFTS is designed to have the resolution and bandwidth coverage of ~3 and ~50 nm, respectively. The resonance peaks from the MRR drop port are reconstructed from the SHFTS, and the resonance wavelength shift due to the refractive index change is retrieved from the reconstructed spectrum with the limit of detection of 0.042 RIU. Our proof-of-concept experiment demonstrates the on-chip biosensing platform without using the external OSA to read the wavelength data and paves the way for a monolithically integrated lab-on-a-chip optical biosensor with the light source/sensor/detector integration.

**Funding.** National Science Foundation (1932753).

**Disclosures.** The authors declare no conflicts of interest.

**Data availability.** Data underlying the results presented in this paper are not publicly available at this time but may be obtained from the authors upon reasonable request.

**Supplemental document.** See Supplement 1 for supporting content.

## REFERENCES

1. A. Asghari, C. Wang, K. M. Yoo, A. Rostamian, X. Xu, J.-D. Shin, H. Dalir, and R. T. Chen, Appl. Phys. Rev. **8**, 031313 (2021).
2. W. Bogaerts, P. De Heyn, T. Van Vaerenbergh, K. De Vos, S. Kumar Selvaraja, T. Claes, P. Dumon, P. Bienstman, D. Van Thourhout, and R. Baets, Laser Photonics Rev. **6**, 47 (2012).
3. P. Steglich, M. Hülsemann, B. Dietzel, and A. Mai, Molecules **24**, 519 (2019).
4. Y. R. Bawankar and A. Singh, in *2021 5th Conference on Information and Communication Technology (CICT)* (2021), pp. 1–6.
5. C.-W. Chang, X. Xu, S. Chakravarty, H.-C. Huang, L.-W. Tu, Q. Y. Chen, H. Dalir, M. A. Krainak, and R. T. Chen, Biosens. Bioelectron. **141**, 111396 (2019).
6. H. Yan, L. Huang, X. Xu, S. Chakravarty, N. Tang, H. Tian, and R. T. Chen, Opt. Express **24**, 29724 (2016).
7. D. Dai, Opt. Express **17**, 23817 (2009).
8. T. Claes, W. Bogaerts, and P. Bienstman, Opt. Express **18**, 22747 (2010).
9. X. Wu, T. Fan, A. A. Eftekhar, A. H. Hosseinnia, and A. Adibi, OSA Continuum **3**, 3390 (2020).
10. Z. Zhang, Y. Wang, and H. K. Tsang, ACS Photonics **8**, 1251 (2021).
11. Z. Zhang, Y. Wang, and H. K. Tsang, IEEE J. Quantum Electron. **56**, 8400308 (2020).
12. E. J. Stanton, A. Spott, M. L. Davenport, N. Volet, and J. E. Bowers, Opt. Lett. **41**, 1785 (2016).
13. N. Ismail, F. Sun, G. Sengo, K. Wörhoff, A. Driessen, R. M. de Ridder, and M. Pollnau, Opt. Express **19**, 8781 (2011).
14. R. Cheng, C.-L. Zou, X. Guo, S. Wang, X. Han, and H. X. Tang, Nat. Commun. **10**, 4104 (2019).
15. X. Nie, E. Ryckeboer, G. Roelkens, and R. Baets, Opt. Express **25**, A409 (2017).
16. X. Chen, P. Huang, N. Wang, Y. Zhu, and J. Zhang, Sensors **21**, 2352 (2021).
17. M. Florjańczyk, P. Cheben, S. Janz, A. Scott, B. Solheim, and D.-X. Xu, Opt. Express **15**, 18176 (2007).
18. D. G. Andrade, T. T. D. Dinh, S. Guerber, N. Vulliet, S. Cremer, S. Monfray, E. Cassan, D. M. Morini, F. Boeuf, P. Cheben, L. Vivien, A. V. Velasco, and C. A. Ramos, Opt. Lett. **46**, 4021 (2021).
19. H. Wang, Z. Lin, Q. Li, and W. Shi, Opt. Lett. **44**, 2923 (2019).
20. E. Heidari, X. Xu, C.-J. Chung, and R. T. Chen, Opt. Lett. **44**, 2883 (2019).
21. K. M. Yoo and R. T. Chen, ACS Photonics **9**, 2691 (2022).
22. D. M. Kita, B. Miranda, D. Favela, D. Bono, J. Michon, H. Lin, T. Gu, and J. Hu, Nat. Commun. **9**, 4405 (2018).
23. B. I. Akca, Opt. Express **25**, 1487 (2017).
24. S. N. Zheng, J. Zou, H. Cai, J. F. Song, L. K. Chin, P. Y. Liu, Z. P. Lin, D. L. Kwong, and A. Q. Liu, Nat. Commun. **10**, 2349 (2019).
25. M. Montesinos-Ballester, Q. Liu, V. Vakarin, J. M. Ramirez, C. Alonso-Ramos, X. L. Roux, J. Frigerio, A. Ballabio, E. Talamas, L. Vivien, G. Isella, and D. Marris-Morini, Sci. Rep. **9**, 14633 (2019).
26. D. Pohl, M. R. Escalé, M. Madi, F. Kaufmann, P. Brotzer, A. Sergeyev, B. Guldimann, P. Giaccari, E. Alberti, U. Meier, and R. Grange, Nat. Photonics **14**, 24 (2020).
27. E. H. Williams, A. V. Davydov, A. Motayed, S. G. Sundaresan, P. Bocchini, L. J. Richter, G. Stan, K. Steffens, R. Zangmeister, J. A. Schreifels, and M. V. Rao, Appl. Surf. Sci. **258**, 6056 (2012).
28. H. Li, S. Zhang, Z. Zhang, S. Zuo, S. Zhang, Y. Sun, D. Zhao, and Z. Zhang, Nanomaterials **10**, 1683 (2020).
29. Y. Wang, X. Wang, J. Flueckiger, H. Yun, W. Shi, R. Bojko, N. A. F. Jaeger, and L. Chrostowski, Opt. Express **22**, 20652 (2014).
30. P. Steglich, C. Villringer, S. Dümecke, Y. P. Michel, M. Casalboni, and S. Schrader, in *2015 International Conference on Photonics, Optics and Laser Technology (PHOTOPTICS)*, Vol. 2 (2015), pp. 47–52.
31. E. Luan, H. Shoman, D. M. Ratner, K. C. Cheung, and L. Chrostowski, Sensors **18**, 3519 (2018).
32. Y. Liu, T. Chang, and A. E. Craig, Opt. Eng. **44**, 084601 (2005).